Check for updates

Microstructure and properties of lightweight $Al_{0.2}CrNbTiV$ refractory high entropy alloy coating with different dilutions deposited by high speed laser cladding

Li-Yan Lou [a,b], Kang-Cheng Liu [a], Yun-Jie Jia [b], Gang Ji [a], Wei Wang [b], Chang-Jiu Li [a], Cheng-Xin Li [a,*]

[a] *School of Materials Science and Engineering, Xi'an Jiaotong University, Xi'an 710049, China*
[b] *National-local Joint Engineering Laboratory of Intelligent Manufacturing Oriented Automobile Die & Mould, Tianjin University of Technology and Education, Tianjin 300222, China*

A B S T R A C T

Light weight $Al_{0.2}CrNbTiV$ refractory high-entropy alloy (RHEA) coatings with different dilutions were deposited by high speed laser cladding technology (HSLC) on TC4 substrate. The effect of key processing parameters on the dilution of HSLC coatings were investigated, and coating with a dilution lower than 3 % could be obtained through the control of specific energy density and specific powder density. $Al_{0.2}CrNbTiV$ RHEA coatings almost free of defects in a thickness from ~150 μm to 450 μm were manufactured with varying dilution of 2.4 %–33.6 %. HSLC facilitated the formation of disordered solid solution, and S—K criterion of S < 6.5 kJ/g, $3.85 \leq K \leq 140$ J/mm² was proposed based on the processing characteristics of HSLC to obtain simple solid solution structured coating in low dilution (<10 %). The HSLC deposited $Al_{0.2}CrNbTiV$ RHEA coatings in typical dilution of 3.1 % and 31.9 % were analyzed, which kept simple BCC solid solution structure, accompanied by an increase in lattice constant with the massively dissolved Ti elements in high dilution coating. Moreover, the $Al_{0.2}CrNbTiV$ RHEA coatings exhibited columnar dominant structure with fine grain size. The coating in high dilution exhibited a stronger tendency for epitaxial growth with increased grain size and lower dislocation density, resulting in a decrease in hardness as well as the resistance to plastic deformation.

1. Introduction

The refractory high entropy alloys (RHEAs) proposed in 2010 have the potential to exhibit high strength at high temperature attributed to the constituent elements with extremely high melting points such as W, Hf, Ta, Zr, Nb, et al. Thus, RHEAs have been considered as the potential next generation high-temperature materials, which may break through the limitation of the operating temperature of the state-of-the-art materials such as nickel-based superalloy [1,2]. However, RHEAs suffer from high density, room-temperature brittleness, especially insufficient oxidation resistance in general. For example, the density of the first developed RHEAs NbMoTaW and NbMoTaWV was high as 13.75 g/cm³ and 12.36 g/cm³, while the fracture strain at room temperature was only about 1.5 % and 0.5 %, respectively [3]. The ductility of the RHEAs could get substantially increased through the proper design of the chemical compositions. Such as the well-known Ta-Nb-Hf-Zr-Ti series RHEAs, the room temperature ductility was improved with the replacement of Mo, W by Hf, Zr and Ti, and Ta20Nb20Hf20Zr20Ti20 presented a ductility ε > 50 % and compression yield stress $\sigma_{0.2} = 929$

MPa [4] at room temperature. And the lightweight $Al_{0.2}CrNbTiV$ RHEA proposed in our previous research [5] showed good combination of strength and ductility at room temperature, enabling deformation in compression to ε > 50 %, with a yield strength of 1570 MPa in a low density of 6.38 g/cm³, by the addition of lightweight elements Al and V.

As HEA coatings could decrease the cost of the bulk alloy and overcome the size limitation of arc melting, and densely fused coating with good metallurgical bonding in a thickness over a wide range from tens micrometer to millimeter could be obtained through laser cladding [6], vast majority of previous studies have focused on laser cladded RHEA coatings. For example, NiTiCrNbTa$_x$ (x = 0.1, 0.3, 0.5, 1) RHEA coatings exhibited excellent corrosion resistance with a minimum corrosion current density of 1.08×10^{-7} A/cm², and the micro-hardness was up to ~922.8 $HV_{0.3}$ [7]. TiZrNbWMo coatings exhibited a superior thermal stability with BCC solid solution remained almost unchanged except secondary precipitated phase formed, and their microhardness increased remarkably from 700 $HV_{0.5}$ in the as-clad state to ~1300 $HV_{0.5}$ after heat treatment at 800 °C [8]. MoFeCrTiWAlNb$_3$ eutectic coating showed excellent high temperature softening resistance [9] and

---

* Corresponding author.
  E-mail address: licx@mail.xjtu.edu.cn (C.-X. Li).

AlTiVMoNb coatings showed superior oxidation resistance compared to the TC4 substrate [10]. However, the dilution occurs inevitably during laser cladding process as the powder fillers and substrate are partially intermixed in the molten pool created by the laser beam to form a metallurgical bonding [11]. The possible dilution could affect the coating properties, including hardness, corrosion resistance [12], even the formability of solid solution of HEAs coating. Li et al. [13] fabricated FeCoNiCrAl HEA coating on Q235 carbon steel. However, inappropriate process resulted in a large dilution to the coating, which resulted in the formation of an FCC phase, and subsequently decreased the hardness of the coating to only ~200 HV. The dilution is even higher than 35 % in the laser cladded FeCoNiCrAl HEA coating produced by Jiang et al. [15]. The high dilution could also be used to alter the coating composition. Liu et al. [14] used Fe atoms from the substrate to fabricate FeCoNiCrAlTi HEA coating, but the results showed that the distribution and concentration of Fe in the coating could not be accurately controlled. However, a weak bonding between the coating and the substrate may be formed if the substrate melting is remarkably reduced to limit the dilution. Therefore, in order to obtain the HEA coating with excellent metallurgical bonding and properties, it was still a great challenge to well control the dilution during laser cladding.

Recently, high speed laser cladding (HSLC) [16,17], a novel additive manufacturing technology with the advantage of higher efficiency, has been developed through optimizing the energy allocations to substrate and powder flow. Hence the thermal impact on the substrate in HSLC is dramatically reduced. Xu et al. [18] prepared $CuAl_xNiCrFe$ HEAs coating with a thickness of about 200 μm using HSLC, and they showed that the element transition zone was only a few micrometers wide, indicating a quite low dilution and decreased thermal effect on the substrate. Lampa and Smirnov [19] compared the microstructure of coatings fabricated using traditional laser cladding and HSLC, suggesting an ultralow dilution rate with HSLC coating. As reported by Li [20] et al., the lower dilution of HSLC resulted in a coating with a higher Cr content, which exhibited a better corrosion resistance than the coating produced by traditional laser cladding. It seems that it is more easily to fabricate the coating with low dilution for HSLC compared with traditional laser cladding. However, for the substrate with low melting point, such as magnesium, copper, the dilution control is also not easy for HSLC. The NiCrBSi self-fluxing alloy coating fabricated by Osama [21] on LA43M magnesium substrate by HSLC has a transition zone of ~100 μm, which is composed of a mixture of magnesium substrate and partially melted NiCrBSi alloy powder, due to the relatively high melting point of NiCrBSi alloy, the unmelted NiCrBSi particles are injected into the molten pool of magnesium substrate thus forming the transition zone. And the formation of the transition zone indicates a high dilution rate of the NiCrBSi coating. Ti-Cu-NiCoCrAlTaY coating on the titanium substrate was fabricated through two steps using HSLC, depositing Cu powder on the titanium substrate at first, then deposting NiCoCrAlTaY powder on the surface of Ti—Cu coating [22]. The uniform coating with the well combination of Cu and NiCoCrAlTaY was obtained, with the elements of Cu, Ni, Co, Cr, et al. uniformly distributed, which indicated the sever dilution of the Ti—Cu coating. The FeCoNiCrAl coatings were prepared by HSLC on C45 carbon steel and 304 stainless steel (304SS) pipes by Du et al. [23], they showed that the dilution was quite different for different substrates, and the transition layers are ~10.4 μm for C45 while 130 μm for 304SS. This fact revealed a more sever dilution for the coating on 3044SS substrate than mild carbon steel substrate. The reason was attributed to much lower thermal conductivity (15.4 $W \cdot m^{-1} \cdot K^{-1}$) of 304SS than that of C45 (49.2 $W \cdot m^{-1} \cdot K^{-1}$). And the low thermal conductivity resulted in a high degree overheating for the 304SS surface. For Ti6Al4V (TC4) titanium alloy, since its thermal conductivity of 6.1 $W \cdot m^{-1} \cdot K^{-1}$ at room temperature (calculated using JMat Pro software) is even lower than 304 stainless steel, it would be more difficult to deposit the coating with low dilution further on its surface even using HSLC technology. Accordingly, it is of essential importance to examine the dilution control strategy for practical applications during

HSLC deposition of the coatings especially on the substrate with low melting point or thermal conductivity.

Herein, a systematic study was carried out to clarify the effect of processing variables on the dilution of the coating on TC4 substrate typically of low thermal conductivity. After that, $Al_{0.2}CrNbTiV$ coating with typical dilution were produced using HSLC technology, and extensively characterized for phase content, microstructure, chemical homogeneity and mechanical properties.

2. Materials and experimental procedures

Commercial Ti-6Al-4 V titanium alloy (hereafter referred to as TC4) rod with a diameter of 30 mm was selected as substrate, which was cleaned with acetone before the experiment. The atomized $Al_{0.2}CrNbTiV$ RHEAs spherical powders (50–150 μm) were used as feedstock powder materials for the deposition of $Al_{0.2}CrNbTiV$ RHEAs coating (Fig. 1), and the compositions of the powder are shown as Table 1.

The 2.5 kW semiconductor laser with fiber coupled output was used as the heat source. The laser focusing spot size is Φ2.5 mm with Gaussian shaped laser beam profile. A home-designed co-axial powder feeding nozzle was used for the laser cladding. The cladding experiment was carried out inside a protective gas box with continuous injection of argon (99.99 %, flow rate 0.5 L/min) to prevent the oxidation of the coating. The coatings were deposited at an overlapping ratio of 70 % with a carrier gas flow rate of 6 L/min, and protective gas flow rate of 1 L/min.

Specimens were cut from the as-prepared coatings with substrates by wire electrical discharge cutting, and then mounted, ground and polished for the observation of the microstructure. Crystal structure and phases of the coatings were characterized with X-ray diffraction (XRD, Bruker D8 ADVANCE A25, Germany). The XRD analysis was performed with Cu-Ka radiation at 40 kV and the scanning speed of 0.02°/s. The microstructure was examined by Hitachi S-3400 Scanning Electron Microscope (SEM) and elemental contents were analyzed with Energy-Dispersive Spectrometer (EDS) attached to SEM. The coating hardness was measured on polished surfaces with a load of 200 gf and a dwell time of 15 s using Vickers microhardness tester (Wolpert Wilson Instruments 401MVD), 5 tests were made for each specimen. The load-displacement relations were obtained by TI950 Triboindenter at room temperature for estimation of the elastic moduli of the coatings. The experiment was conducted at peak load of 9 mN with a loading time of 2 s, and the loading and unloading time was placed at 20 s. And three specimens were selected for each coating, with each specimen three points to calculate the mean value and synthesize the nano-indentation curve. The EBSD characterization of the coatings was performed using the HKL system equipped in a LEO1450 scanning electron microscope
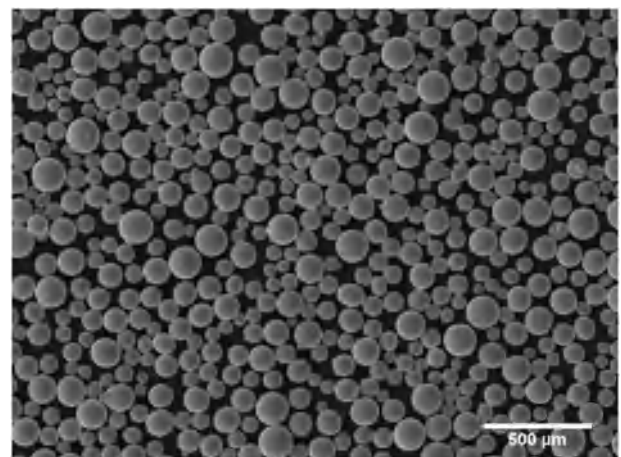

Fig. 1. SEM of $Al_{0.2}CrNbTiV$ RHEA powder.

Table 1
Chemical compositions of $Al_{0.2}CrNbTiV$ RHEA powder (at.%).

Element	Al	Cr	Nb	Ti	V
Nominal compositions	4.76	23.81	23.81	23.81	23.81
Test compositions	5.1	23.73	24.72	23.01	23.44

from the cross section with a given step size of 0.65–0.8 μm. EBSD data was processed subsequently by Channel 5 software, and the external load of Schmid factor maps is Z-axis, consistent with the direction of nano-indentation.

3. Results and discussion

3.1. Effect of processing parameters on dilution of HSLC coating

During HSLC process, the HEA coating will experience the complex local thermal history with rapid solidification rate (10^3–10^6 K/s) and large thermal gradients (10^5–10^7 K/m) [11] with possible dilution by the substrate, which may affect their phase stability. The dilution of the coating mainly originates from the melting of the substrate. Generally, the dilution increases with increasing laser power and typically decreases with laser scanning speed. Thus, the specific energy density K given below is used as a typical parameter for examining the processing parameters on the dilution [24]:

$$K = \frac{P}{D \cdot v} \tag{1}$$

where P is the laser power, D is the laser beam spot diameter on the substrate, v is the scanning speed. The cladding at a high K value may cause the strong melting of the substrate, and deteriorate the properties of the coating. On the other hand, the test at a too low K value could cause weak bonding between the coating and the substrate and increase the formation tendency of the amorphous phase correspondingly.

Different from the traditional laser cladding process, during HSLC process, a larger amount of laser energy is absorbed by the powder particles. Thus the powder particle temperature could reach the range of the melting point before being guided into the melt pool [25]. On the contrary, the portion of laser energy absorbed by the substrate is much smaller than that in the traditional cladding process. Since the powder stream has a stronger shielding effect to the laser energy on the substrate, and subsequently influences the dilution of the coating, a synthetic factor defined as the specific powder density M is proposed to evaluate the effect of the powder flow [26]. M can be expressed as following Eq.(2):

$$M = \frac{F}{D \cdot v} \tag{2}$$

where M is the specific powder density, F is the powder flow rate, D is the powder flow beam spot diameter, v is the scanning speed. In order to deposit coating with relatively low and high dilutions, the cladding experiments were carried out in a wide range of processing parameters as shown in Table 2. And Fig. 2 shows cladding condition map depicted using the specific energy density K and the specific powder density M to examine their effect on the coating features. Fig. 3 shows the cross-sectional microstructures of the typical coating-cladded specimen at different processing parameters. Since all the coatings shown in Fig. 3 were cladded by one pass with an overlapping of 70 %, the relative thickness presents the relative cladding efficiency. It was found that under present experimental condition range, the cladding failed to form the coating under a specific laser energy of 3.19 J/mm². For all coatings, the dilution and coating-substrate bonding for each cladded coating are estimated based on the EDX element content analysis results using the following equation [27,28]:

$$dilution = \frac{\rho_p(x_c - x_p)}{\rho_s(x_s - x_{coating}) + \rho_p(x_c - x_p)} \tag{3}$$

where ρ_p is the density of melted powder alloy, ρ_s is density of substrate material, X_c is weight percent of element X in the whole coating, X_p is the weight percent of element X in the powder alloy, and X_s is the weight percent of element X in the substrate [28,29]. Cr and Nb elements are used in Eq.3 to calculate the dilution for the individual element, and the average values are calculated as the dilution values of the coatings and are shown in Table 2.

A successful applications of HEA coating requires metallurgical bonding with the dilution as low as possible. A higher cladding rate with high powder deposition and power efficiency is also desirable from the economic points of view. The present results reveals that the coating thickness increases with increasing the specific energy K for a given M, since more laser power is used for melting the powder as shown in Fig. 3. On the other hand, the data in Table 2 reveals that dilution is also increased with increasing K, that is, a high laser energy could lead to a dilution, under the conditions of No.5 and No.8 in Table 2, the coatings are cladded at high dilution as 31.9 % and 33.6 %. But the increased K value doesn't mean the increasing of powder using efficiency, it has been reported [11], the excessive increased K has no remarkable enhancement in powder efficiency, since there is no obvious improvement in the conversion of powder feedstock to cladding, and the energy efficiency could get decreased instead. Conversely, under a given K, the larger powder flow density M is conducive to decrease the dilution of the

Table 2
Process parameters of coatings with different K/ M value and dilution.

No.	Laser power (kW)	Deposition speed (mm/s)	Powder flow rate (g/min)	Overlapping ratio (%)	K (J/mm²)	M (10^{-4} g/mm²)	S (KJ/g)	Dilution (%)
1	1.5	314	27.78	70	2.39	7.37	3.24	/
2	1.5	157	14.16	70	4.78	7.52	6.36	5.1
3	1.5	157	27.78	70	4.78	14.75	3.24	3.1
4	1.5	157	27.78	70	4.78	14.75	3.24	2.4
5	2	157	14.16	70	6.37	7.52	8.47	31.9
6	2	157	23.22	70	6.37	12.32	5.17	8.0
7	2	157	27.78	70	6.37	14.75	4.32	6.0
8	2.5	314	14.16	70	3.98	3.76	10.59	33.6
9	2.5	157	23.22	70	7.96	12.32	6.46	9.8
10	2.5	157	27.78	70	7.96	14.75	5.4	8.8
11	1.5	235	23.22	70	3.19	8.23	3.88	/
12	2	314	23.22	70	3.18	6.16	5.16	/
13	2	235	14.16	70	4.26	5.02	8.49	18.1
14	2	235	23.22	70	4.26	8.23	5.18	6.1
15	2	235	27.78	70	4.26	9.85	4.32	5.5
16	2.5	235	27.78	70	5.32	9.85	5.4	7.3
17	2.5	314	14.16	70	3.98	3.76	10.59	24.6

Note: the dilution of the discontinuous coating is not calculated with "/" represented.
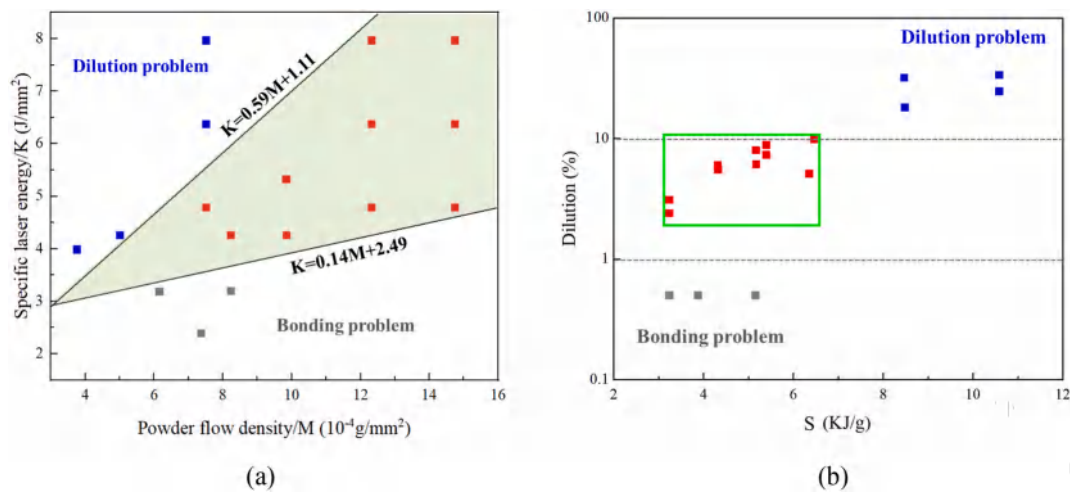
Fig. 2. Cladding condition map of HLSC coatings with (a) represents the relationship of dilution and specific energy density & powder flow density and (b) represents the relationship of dilution and S value.
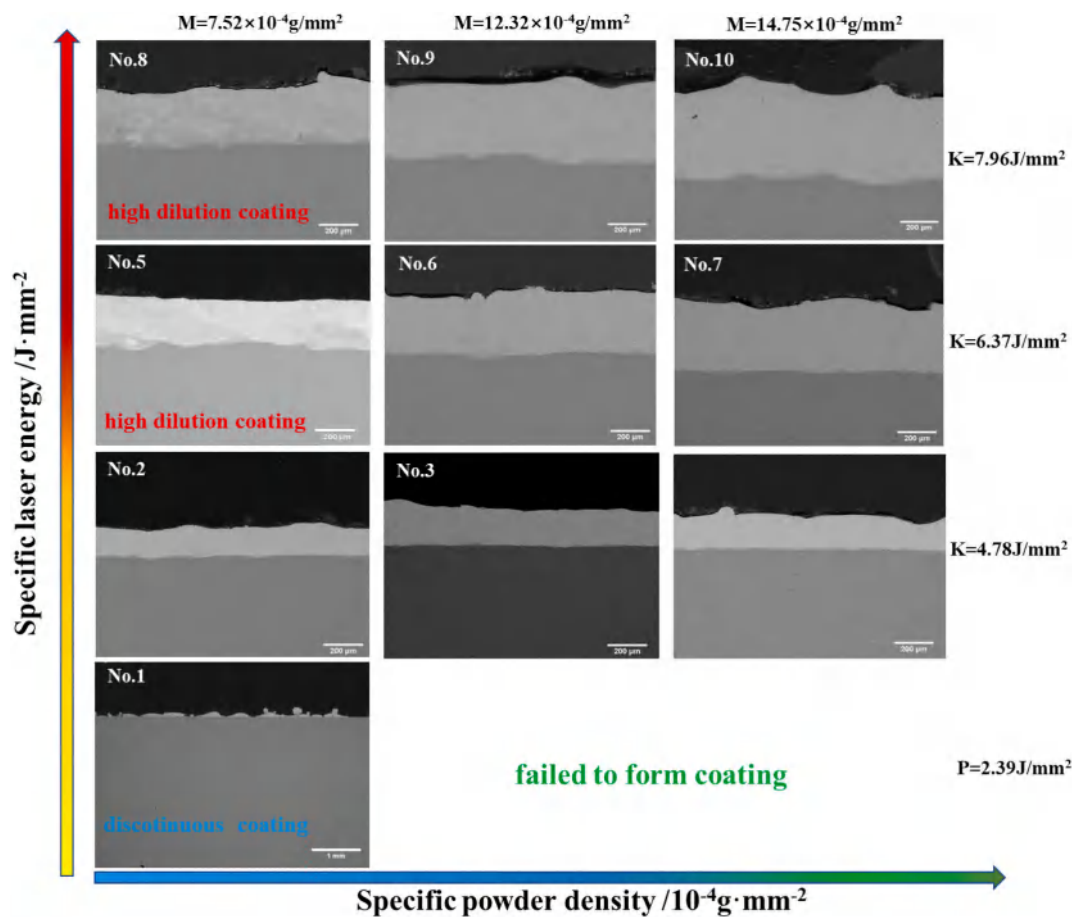

Fig. 3. Change of the cross-sectional microstructure of the coatings cladded with the specific laser energy and specific powder density.

coating as more laser energy absorbed by the powder beam, and the coating thickness could get increased to some extent simultaneously. But the laser energy can't melt the powder thoroughly if too much powder injected. Such as No.4 coating has a closely thickness to No.3, though its powder flow is larger, indicating the energy is insufficient for the given M, and the extra powder, which is not conversed to cladding all get wasted, despite the dilution is decreased slightly. If further increasing the powder flow density, the bonding problem will appear due to the

insufficient laser energy on the substrate. For instance, No.1 coating is discontinuous as the powder flow density is too high for the given K. And the powder even can't be deposited to form a coating if the powder flow density continues to increase.

In order to control the dilution of laser cladded coating, Oliveira et al. [30]. proposed a combined parameters $\sqrt{Pv/f}$, and Qi [11] proposed an optimized parameter $\sqrt{Pv/Df}$ considering the effect of laser beam diameter D. However, no linear relationship between Pv/f or

$\sqrt{Pv/Df}$ and dilution is found here, perhaps due to the relatively small data volume in the current study or the much higher depositing speed of HSLC. In the current research, the dilution is correlated with the combined parameter of K and M, under a given M, the K has a maximum value before dilution occurs, also minimum energy is required in case the coating starts to be discontinuous or bonding problem occurs. The critical state exists, where coating with dilution >10 % is considered to be high dilution coating in current research as low dilution is one of the advantages of HSLC. And the critical correlation between K and M is summarized approximately through the processing results as shown in Fig. 2a. A linear relationship is found to exist between parameter P and M, in the region above K = 0.59 M + 1.11, coating with high dilution will be obtained, whereas, in the region below K = 0.14 M + 2.49, coating will have bonding problem. Fig. 2a also shows the hatched area that the cladding process is feasible.

In order to reveal the combination effect of K and M more directly, a synthetic factor S is proposed, which could be calculated by the following Eq.(4):

$$S = \frac{K}{M} = \frac{P}{F} \tag{4}$$

Fig. 2b indicates the relationship between dilution and S, where the dilution of No. 1, No.11 and No.13 coatings with bonding problem is assigned as 0.5. A higher S value means more laser energy P is absorbed by the substrate with a given powder flow F, but the dilution problem will occur correspondingly, similar to the effect of K. Fig. 2b reveals dilution problem occurred with S>8.5 kJ/g. Thus, a suitable S value could avoid a dilution coating. However, weak bonding could still be obtained with a too low K value, for the heat input may be not enough to melt the substrate to form metallurgical bonding, for example, No. 1, No.11 and No.13 coatings with S< 6 kJ/g all have bonding problem under a K of 3.19 J/mm². as seen in Fig. 2b. Only the coatings involved in the rectangle region (S < 6.5 kJ/g) exhibit low dilution (1 % ~ 10 %) and strong metallurgical bonding. Therefore, S value should be controlled below a certain value and matched with appropriate K value, and S—K criterion (S < 6.5 kJ/g, K>3.2 J/mm²) could be proposed to hinder the dilution and weak bonding problem of HSLC coating. In this research, through the unique combination of processing parameters, successful control of dilution for the ~150–450 μm thick HEA coatings are obtained successfully.

3.2. Phase structure analysis of Al$_{0.2}$CrNbTiV coatings with different dilutions

No. 3 and No. 5 coatings in Table 2 are chosen to analyze the factors influencing the dilution, and are denoted as LC1.5 and LC2.0 in this research. The XRD patterns of the Al$_{0.2}$CrNbTiV RHEAs coatings and the same bulk alloy in the as-cast state are shown in Fig. 4. The bulk alloy was fabricated by vacuum arc melting as reported in our previous investigation [5]. The XRD results show that the same characteristic peaks are observed for the Al$_{0.2}$CrNbTiV RHEAs coatings and cast bulk. Both the coating and the bulk alloy are presented in the single BCC phase structure, indicating no phase transformation occurred during the HSLC process. In addition, it is observed that a little shift of the diffraction peaks of the coating to small diffraction angle occurred compared with the as-cast alloy. This could be attributed to the lattice distortion and the macro residual stress [31,32] of the coating. The lattice constant can be estimated according to the Bragg's law in Eq.(5):

$$a = \frac{\lambda}{2 sin\theta} \sqrt{h^2 + k^2 + l^2} \tag{5}$$

where a is the lattice constant, θ is the Bragg angle, λ is the wavelength of X-ray beam as 0.15406 nm, and (hkl) is the crystal plane index. The strongest diffraction peak is selected for the estimation to avoid errors caused by weak diffraction peaks. The estimated lattice constants of
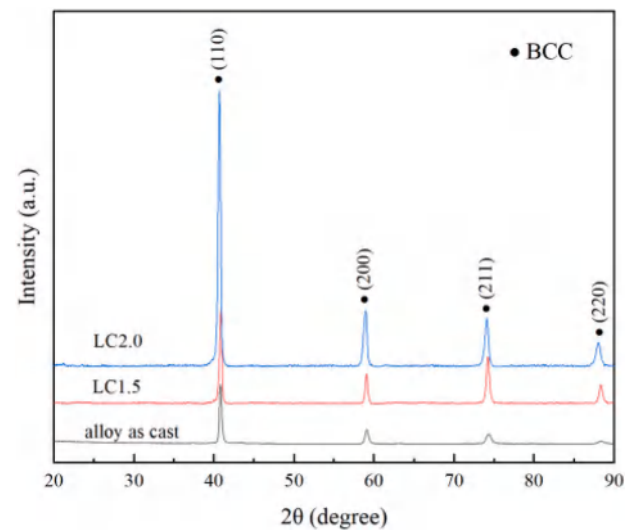

Fig. 4. XRD patterns of Al$_{0.2}$CrNbTiV coatings for different parameters.

LC1.5 and LC2.0 are 3.126 Å and 3.136 Å, respectively. Both values are larger than 3.124 Å estimated for the as-casted Al$_{0.2}$CrNbTiV alloy reported in our previous research [5]. The result is closely related to the different processing characteristic of laser cladding from traditional casting process. The molten pool is rapidly cooled and solidified in an extremely short time during laser cladding, which can effectively inhibit the long-range diffusion of the metal atoms [33,34]. Consequently, elements with different atomic radius have no enough time to diffuse and will be retained in the supersaturated BCC solid solution, leading to the enhancement of the lattice distortion and the increase of the residual stress. Furthermore, with HSLC, the rapid cooling effect can be further intensified, since its cooling rate could be one order of magnitude higher than the traditional laser cladding. Hence the resultant coatings have a larger lattice constant than the bulk alloy. Moreover, LC2.0 has higher Ti concentration of ~40 at.% with high dilution (shown in Table 5). Ti atom, of larger atomic radius could occupy more positions in current BCC structured Al-Cr-Nb-Ti-V solid solution during the solidification process, increasing the lattice constant. It seems that the additional Ti is predominant over the cooling rate, making LC2.0 have a larger lattice parameter than LC1.5.

As a result of the dilution of the substrate, the coating composition deviates from the nominal design, resulting in a change in mixing entropies ΔS$_{mix}$ of the alloy system. Consequently, this may affect the stability of the disordered solid-solution. And our previous work had proved the precipitation of the secondary laves phase in the Al$_x$CrNbTiV RHEAs will result in a complete loss in ductility of the alloys [5], so that it is meaningful to obtain a single solid solution structured coating. Solid-solution formation criteria ΔH$_{mix}$, ΔS$_{mix}$, δ, Ω and VEC had been proposed based on Hume-Rothery rules [35,36]. Here, ΔH$_{mix}$ is mixing enthalpy, ΔS$_{mix}$ is mixing entropy, δ is atomic radius difference, Ω is single-phase ability (defined as T × ΔS$_{mix}$/|ΔH$_{mix}$|) and VEC is valence electron concentration, which can be calculated with $VEC = c_i \sum VEC_i$ [37]. A combination of $-20 \leq$ ΔH$_{mix} \leq 5$ k J/mol, $12 \leq$ ΔS$_{mix} \leq 17.5$ J/K·mol, and δ ≤ 6.4 %, Ω ≥ 1.1 is proposed for solid solution stability by Zhang et al. [38] and Yang et al. [39,40]. Guo et al. [41] suggested that BCC phases will be more stable if VEC ≤ 6.87. Considering the different processing characteristic between laser cladding and traditional arc melting process, Juan et al. proposed [34] a modified criterion specially targeting the multi-component laser-clad coating based on considerable data obtained from numerous laser cladded HEAs coating as: $10.8 \leq$ ΔSmix ≤16.2 J/K·mol, $-17 \leq$ ΔHmix ≤7 k J/mol, and $0 \leq δ \leq 14$ %, and the specific energy density K was also supplemented as a part of the criterion as: $40 \leq$ K ≤ 140 J/mm².

The calculated criteria (seen in Table 3) suggests that LC1.5 and

Table 3
The calculated criterions of the $Al_{0.2}CrNbTiV$ coatings.

Alloys	$\Delta S_{mix}/$ J·K^{-1}·mol^{-1}	$\Delta H_{mix}/$ kJ·mol^{-1}	Ω	$\delta/\%$	VEC	K/ J·mm^{-2}
Design	12.57	−7.21	3.34	6.21	4.9	/
LC1.5	12.67	−7.59	2.48	6.14	4.88	4.78
LC2.0	12.04	−8.53	2.56	5.93	4.61	6.37

LC2.0 could fulfill mostly all of the criterions except for K value. However, a single BCC structure is still obtained for both of the coatings, indicating the *K* criteria may be not appropriate for HSLC coating. This should be related to the higher deposition speed of HSLC, being 157 mm/s in the current research and ten times higher than the typical deposition speed of the traditional laser cladding process, which is <2 m/min reported in the most documents [25]. Since the deposition speed of HEAs coating in HSLC is always higher than 100 mm/s [42–48], this results in a substantial low *K* value exceeding the scope of the *K* criterion for traditional laser-clad coating. However, a lower *K* value also means a higher solidification rate as the energy accumulated is less, and the heat dissipation is faster, thus HSLC represents a far more rapid non-equilibrium solidification process. It has been proposed that the multi-alloying elements with different atomic radius increase the solid-liquid-interface energy during the solidification process [49,50], and increase the difficulty of the long range diffusion of atoms. In a rapidly cooling process, the time available for the solute atoms to diffuse from the solvent lattice is much limited, which restrains the nucleation and growth of the intermetallic compounds. And such feature promotes the formation of the solid solutions with severe super-saturation [34]. Aziz et al. [51] also pointed out the rapid cooling is beneficial for the formation of the solid solutions when the solidification rate is higher than the atomic diffusion rate in the intermetallic compound super-lattice. Therefore, rapid heating and cooling during the laser cladding process could enhance the sluggish diffusion effect of HEA, and is more conducive to the formation of the solid solution structure [33,52]. Accordingly, all the HEAs coatings deposited by HSLC reported to now exhibited solid solution structure with *K* value lower than 40 J/mm² (3.85–40 J/mm², 18, 53–55], as shown in Fig. 5, with calculated results listed in Table 4. Thus, the *K* criterion could be expanded to $3.85 \leq K \leq$ 140 J/mm² for the formation of the solid solution structure.

With the combination of S & K range ($S < 6.5$ kJ/g, $K > 3.2$ J·/mm²) to hinder the dilution and weak bonding problem and the K criterion for solid solution stability, a new *S—K* criterion could be proposed as $S < 6.5$ kJ/g, $3.85 \leq K \leq 140$ J/mm² for HSLC to obtain the solid solution
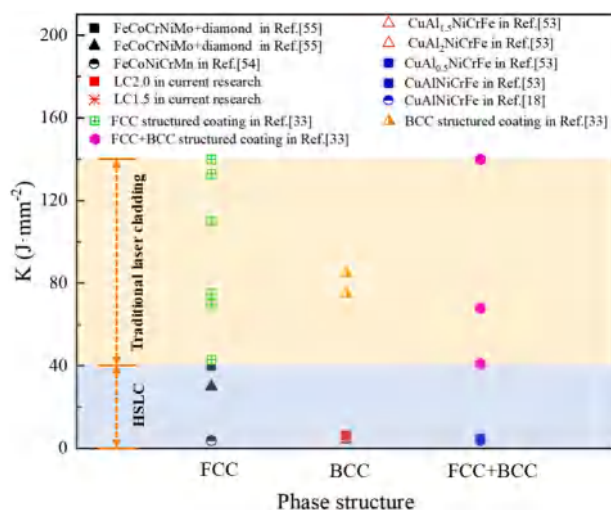
Table 4
The calculated K criterions of the HEA coatings related to HSLC from the publicly reported references.

Substrates	Coatings	Phase	K/ J·mm^{-2}	Refs.
Inconel718	CuAlNiCrFe	FCC + BCC	3.85	[18]
Inconel718	CuAl0.5NiCrFe	FCC + BCC	4.81	[53]
Inconel718	CuAlNiCrFe	FCC + BCC	4.81	[53]
Inconel718	CuAl1.5NiCrFe	BCC	4.81	[53]
Inconel718	CuAl2NiCrFe	BCC	4.81	[53]
45 steel	FeCoNiCrMn	FCC	3.85	[54]
42CrMo steel	FeCoCrNi-Mo HEA/ diamond	FCC FCC	30 40	[55] [55]
Ti-6Al-4 V	LC1.5	BCC	4.78	In this research
Ti-6Al-4 V	LC2.0	BCC	6.37	In this research

structured HEA coating with low dilution (<10 %) and strong bonding. However, it should be noted that, due to the limited number of HEAs coatings specimens deposited by HSLC, this criterion may get modified with more researches conducted in the future.

LC1.5 in lower dilution has a higher ΔS_{mix}, and promotes the formation of random solid-solution, since high ΔS_{mix} could effectively increase the extent of confusion of multi-principal elements alloy system and significantly lower the ΔG_{mix} [40], and elements in LC1.5 could distribute more randomly in the crystal lattice under a larger ΔS_{mix}. However, LC2.0 still possesses single BCC solid solution structure, though its ΔS_{mix} is lower. And this should be associated with the chemical composition of the coating and the dissolved elements from the substrate. Since Ti could act as BCC solid solution stabilizing element due to its closely atomic radius to Al, Nb and the BCC structure of β-Ti, LC2.0 could still maintain the BCC structure despite the Ti concentration of the coating got increased greatly under a high dilution.

3.3. Element distribution and solidification behavior of $Al_{0.2}CrNbTiV$ coatings with different dilutions

The coatings cladded with different heat inputs present dense structure with the thickness of ~180 μm for LC1.5 and ~220 μm for LC2.0, without visible cracks and bonding defects at the interface, as shown in Fig. 6. The fusion line can be clearly identified between the coating and the substrate, indicating the formation of good metallurgical bonding. It is observed that LC2.0 presented a wavy fusion line due to penetration of melting front into the substrate deep during cladding.

The chemical compositions of the coatings are shown in Table 5. The content of Ti elements of LC2.0 under higher heat input reaches 42.28 at.%, deviates from the powder composition sharply, while the composition of LC1.5 has no obvious change. Fig. 7 displays the EDS elements distribution of coatings. Fig. 7c reveals that Ti element segregated obviously in LC2.0 as a result of the massively dissolved Ti from the substrate and the Maragoni convective effect of the molten pool. Meanwhile, the distribution of element Cr, Nb and V of LC2.0 also get affected since rare time is left for the thoroughly mixture and diffusion for the melted powder and substrate. Whereas, elements distribution is relatively uniform in LC1.5, as shown in Fig. 7a. As thermal effect is the main reason of the dilution, LC1.5 is in a low dilution of 3.1 %, while LC2.0 could be high as 31.9 %.

Nb content is used as a calibration for cross-section elemental dilution, and EDS results from Fig. 7b and Fig. 7d indicate that Nb content gradually decreased from the coating to the substrate due to the dilution effect, further proved the formation of strong metallurgical bonding between the coating and substrate. The thickness of the transition zone is ~7 μm for LC2.0, and decreased to ~2 μm for LC1.5 under lower heat

Fig. 5. The effect of K on solid solution formability in HEA coatings fabricated by laser cladding.
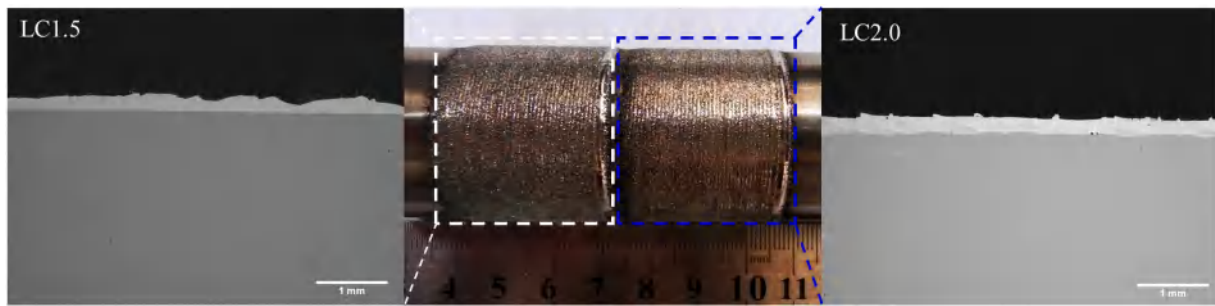
Fig. 6. The macroscopic and cross-sectional morphology of Al$_{0.2}$CrNbTiV coating.

Table 5
Elemental distributions at different regions of LC1.5 and LC2.0 coating (at.%).

| Coating	Region		Al	Ti	V	Cr	Nb
	The whole coating		5.21	23.86	23.85	23.06	24.02
	The bonding region	Grains	5.28	22.84	22.86	20.28	28.74
		Intragranular	4.79	24.80	21.58	25.85	22.99
LC1.5	The middle region	Grains	5.88	22.74	23.41	22.80	25.18
		Intragranular	5.11	24.49	22.34	26.40	21.66
	Coating surface	Grains	4.89	23.68	24.13	23.31	23.99
		Intragranular	4.97	23.96	23.32	24.85	22.92
	The whole coating		6.81	42.28	17.10	16.67	17.14
	The bonding region	Grains	6.78	43.37	17.88	14.00	17.96
		Intragranular	6.86	43.47	16.51	17.25	15.92
LC2.0	The middle region	Grains	7.47	49.29	14.91	13.08	15.26
		Intragranular	7.32	50.24	14.43	14.65	13.37
	Coating surface	Grains	6.11	32.30	20.39	19.66	21.55
		Intragranular	6.18	33.36	19.45	20.72	20.29
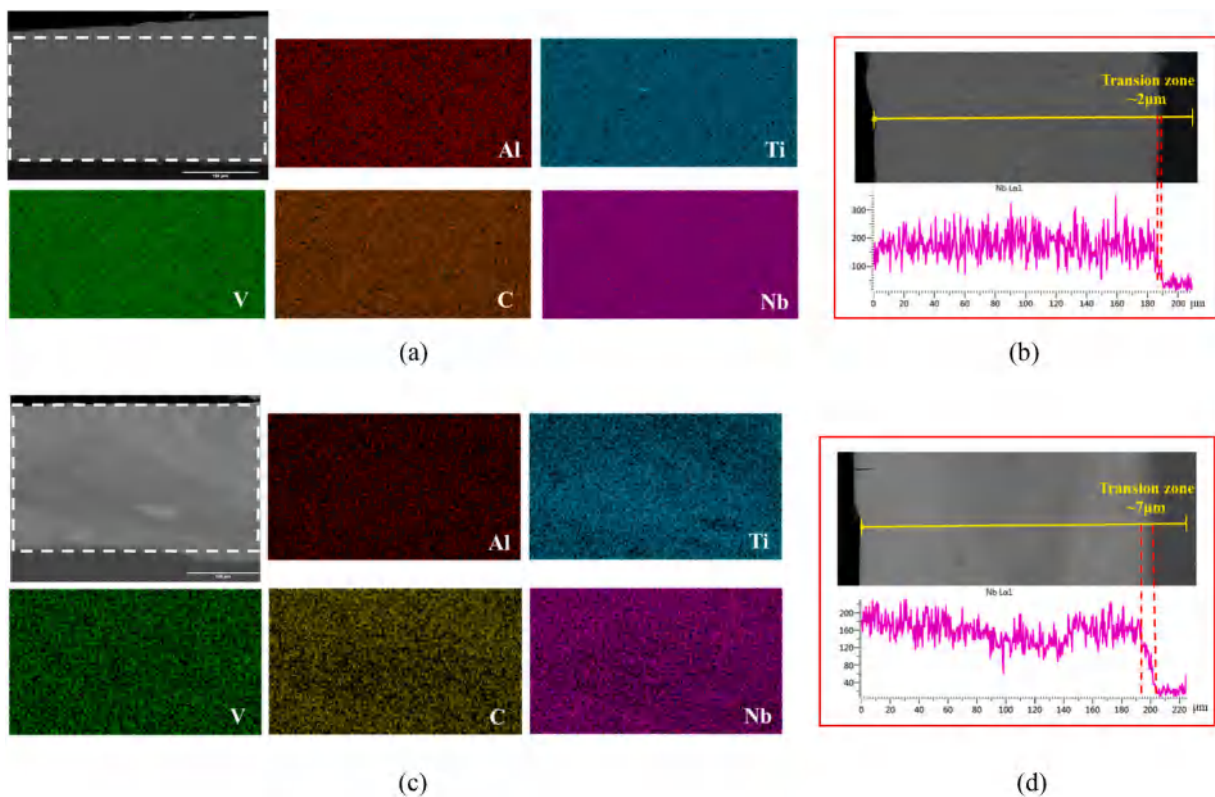
Fig. 7. Element distribution of Al$_{0.2}$CrNbTiV coating: (a) and (c) EDS map of LC1.5, LC2.0, (b) and (d) EDS along linear scanning of LC1.5, LC2.0.
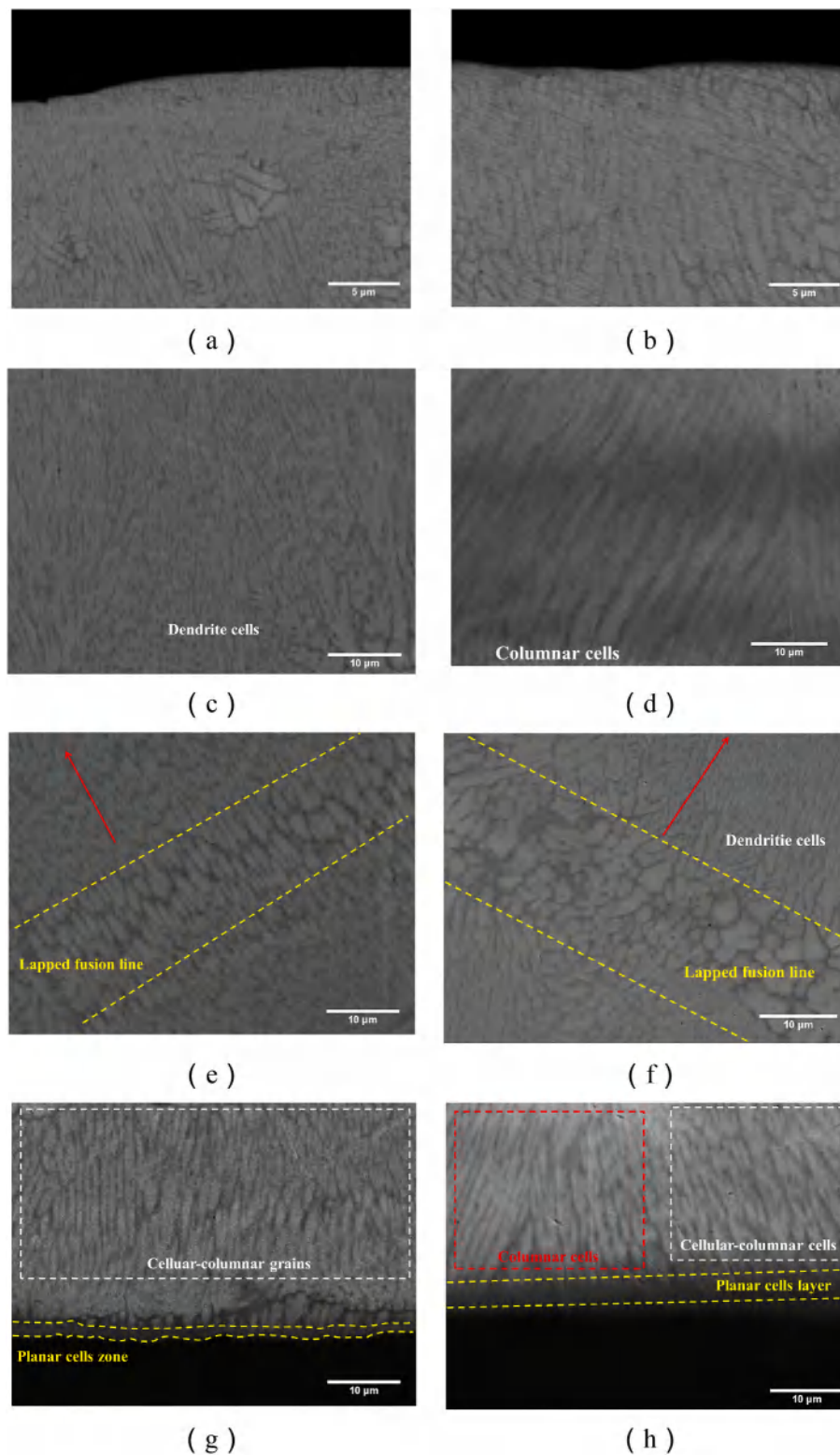
Fig. 8. Cross-sectional microstructure of Al$_{0.2}$CrNbTiV coating: (a)–(e) LC1.5, (f)–(h) LC2.0, with (a) (b) and (f) represent the region near the coating surface, and (b) is the magnification of (a), (c) (d) and (g) represent the clapped region and the middle of the coating; (e) and (h) represent the bonding region.

input, both are smaller than the previous reported laser cladded HEA coatings [11,12], suggesting the controlled thermal effect to the substrate using HSLC.

Fig. 8 depicts the microstructure of the coating at different positions. Both LC1.5 and LC2.0 show single phase structure with no second phase founded, consistent with XRD results. It's know that the solidification structure of a given alloy [56,57] primarily depends on the temperature gradient G and solidification velocity R, with G as the driving force. For laser cladding process, from the bottom of the molten pool to the top, G decreases gradually, R increases continuously, and the solid/liquid interface morphology of the traditional laser cladded coating will normally change from planar to columnar, and then to equiaxed

correspondingly [56,57].

G is affected by process parameters, when a low laser power or a high scanning speed is given, the laser energy input will be reduced, and leading to the decrease of G [58]. Thus, LC1.5 in lower laser power and stronger powder stream has a lower G. During HSLC process, the molten pool solidified from the bottom near the substrate. As the local temperature is extremely high, no constitutional supercooling zone could be formed in front of the solid-liquid interface, and the solidification structure will grow as planar cells with smooth interface and no solute segregation. Noted that, the planar cells layer width of LC2.0 is about 3–4 μm, wider than that of LC1.5, which is <2 μm, as shown in Fig. 8g and Fig. 8h, the reason should be related to the higher G of LC2.0, which is more conducive to the growth of planar cells. However, the planar growth is unstable with the decreasing of G and increasing of R, the solidification cells with epitaxial growth morphology will be formed as the release of the latent heat at the solidification interface and the effect of constitutional undercooling at solidification front. So that, the solidification structure grows as columnar or cellular cells above the planar layer for LC1.5 and LC2.0 in the direction of heat flow (shown in Fig. 8g and Fig. 8h). And columnar cells with a high aspect ratio can be observed in LC2.0 (shown in Fig. 8d) due to a higher temperature gradient and relative stable alloy concentration.

With a relatively lower R, both LC1.5 and LC2.0 continuous to grow in epitaxial growth characteristic steadily in the middle of the coating. However, with the heat accumulation and the release of crystallization latent heat, the decrease of G gets aggravated, whereas, R gets increased gradually. When G/R is insufficient to maintain the growth of the columnar structure, columnar dendrite structure with slight branches will be formed locally [59] (shown in Fig. 8c and Fig. 8f), different from the microstructure of traditional laser cladded coating, the dendritic growth direction is slightly changed for both of the coatings, meaning the inhibition of the growth of secondary dendrite arms. It should be noted that, lapped fusion "line" exists in the coating, with a width of ~13.5 μm for LC1.5 and ~16 μm for LC2.0 (shown in Fig. 8e and Fig. 8f), as LC2.0 has a higher heat input. Above this area, solidification structures grow approximately perpendicular to the lapped fusion line along the heat dissipation direction. The formation of the fusion "line" is related to the multiple heating process of the coating in the vertical direction, since HSLC coating is formed through "dominoes" lapped cladding track [20] with cladding ratio high as 70 %–90 %. It can be seen that, equiaxed crystals are formed there, with grain size a little coarser due to the multiple heating process. However, despite the solidification cells are coarse in the fusion line, the grain size is much smaller compared to conventional laser cladding coating, with ~1.5 μm for LC1.5 and ~2.4 μm for LC2.0, while the typical grain size of conventional laser cladded coatings can reach 20–75 μm [11,15,24,32].

Fine size cells are formed in the upper region of the coating with higher R and greater heat loss velocity, seen in Fig. 8a and Fig. 8b, since the molten pool could contact with the atmospheric environment directly. Generally, fine equiaxed cells will be formed in the upper surface, especially for coatings of traditional alloys, such as nickel/ iron based coating [60]. However, columnar dendrites with unidirectionally orientation are still dominant near the coating surface for LC1.5 and LC2.0. Noted that LC1.5 has more percent of equiaxed cells with lower G, and the cells size is also smaller than LC2.0. And the columnar dendrites dominant solidification structure have been reported in the previous laser processing AlCoCrCuFeNi, FeMnNiCoCr HEA coatings [61–64].

The chemical compositions at different regions of the coating are shown in Table 5, and elements distribute more uniformly in LC1.5, consistent with the EDS map in Fig. 7. The results also indicate that Cr elements tend to segregate at grain boundaries, while more Nb and V elements prefer to gather within the grains. And the reason is related to the highest melting point of Nb and V in the Al-Cr-Nb-Ti-V series alloys (the melting point of element Ti, Cr, Al, Nb, and V is 1668 °C, 1860 °C, 660 °C, 2477 °C, and 1902 °C, respectively), which will precipitate

firstly and gather in the granular regions, as element distribution of the coating is determined when temperature is lower than the melting point [65]. Meanwhile, high lattice distortion will be formed around Cr atoms, since its atomic radius deviates greatly from others (atomic radius of element Ti, Cr, Al, Nb, and V was 1.462 Å, 1.249 Å, 1.432 Å, 1.500 Å, and 1.316 Å, respectively). Thus, Cr tend to be repelled by other atoms during solidification process though Cr has a quite high melting point. Furthermore, the estimation of the solution effect suggests the atomic misfit and modulus misfit around Cr is much higher in Al-Cr-Nb-Ti-V alloys [5]. Moreover, the previous research indicated that the solubility of Cr elements in Al-Cr-Nb-Ti-V(—Zr) BCC disordered solid solution may be lower, since Cr enriched laves phase was easy to precipitate in RHEAs, such as Cr_2Nb type C14 laves phase in AlCr1·5NbTiV [66] and AlCrNbTiV alloys [67], Zr-Cr-Al type C14 laves phase in $Al_xCrNbTiVZr$ ($x = 0.25, 0.5, 1$) alloys [68]. When Cr atoms move into the loose grain boundary, the distortion energy and the internal energy of the coating could get relaxed to some extent, increasing the stability of the BCC solid solution and inhibiting the precipitation of laves phases.

It is interesting to find the solidification structure appearing dark-grey fully or partially separates (surrounds) the structure in light-grey, that is, a relatively thick grain-boundary (GB) layers appear in $Al_{0.2}CrNbTiV$ RHEA coatings. These thick GB layers are liquid during cooling in the Solid + Liquid area of the HEA phase diagram and crystallize as a second solid phase later, which are formed due to the phenomenon of complete or partial GB wetting, with the complete GB wetting means each grain fully embedded in the matrix without touching the other solid grains. Straumal et al. [69,70] indicated that GB wetting phase-transition temperature (T_w) exists in both binary and HEAs, if the solidification route insects the T_w line, the GB energy is higher, complete or incomplete wetting of GBs could be formed, and leading to the thick interlayers.

For $Al_{0.2}CrNbTiV$ RHEA coatings, the primary grains of bcc phase are surrounded by Cr enriched 100–300 nm thick interlayers, demonstrating the wetting of GBs during the solidification process. And the similar phenomenon that the major phases separated by the rather thick layers formed by the minor melt phase (which later crystallizes) was also observed in $MgMoNbFeTi2Y_x$ ($x = 0, 0.4 \%, 0.8 \%, 1.2 \%$) HEA laser cladded coatings [71], with BCC matrix grains rich in Mo and Ni surrounded by the interlayers of Mg, Ti-rich phase. And almost all BCC grains were separated from each other by the Mg, Ti-rich 200–300 nm thick layers. The Mo,Ni-rich BCC-phase (matrix grains) were also surrounded by the interlayers of Mg,Ti-rich phase in $Al_xMo0.5NbFeTiMn$ ($x = 1, 1.5, 2$) HEA laser cladded coatings [72].

And the GB wetting phenomenon is more obvious especially in the lapped fusion line, which may be the reason that the local slower cooling speed make second Cr component has more chance of redistributing. At the same times, in the lapped fusion line of LC2.5 (as seen in Fig. 8f), a great amounts of BCC cells are separated from each other, while for LC2.0 (as seen in Fig. 8e), only few GBs are partially wetted by the melt, which should be related with the chemical composition of the coating, since slight modification of the composition can strongly change the morphology of phases and influence the overall mechanical properties [73] by shifting the position of GB wetting tie lines [69]. And it has been proved in $CoCrFeNiTa_x$ [74], for $CoCrFeNiTa_{0.1}$ and $CoCrFeNiTa_{0.25}$, the matrix has FCC structure, and GB layers contain the Laves phase formed after solidification, but few completely wetted GBs exist in $CoCrFeNiTa_{0.1}$, nearly all GBs are wetted in $CoCrFeNiTa_{0.25}$. However, the influence of such interlayers on HEA properties is not clearly, which need further research in the future.

With the gradually decreased G and increased R, equiaxed crystals dominant solidification structure is easy to form near the surface of laser processing coatings [61,63]. However, columnar grains are dominant in the upper region of the $Al_{0.2}CrNbTiV$ coatings (seen in Fig. 8), in LC2.0, solidification structure near the coating surface even exhibits obvious characteristics of epitaxial growth. And the reason should be related to the columnar to equiaxed transition (CET) phenomenon. In the widely

recognized Hunt's model [75,76] about CET, the decreased degree of undercooling could reduce the critical G for the formation of columnar. And it has been reported [60,64], the sluggish diffusion kinetics could lead to a reduction of the degree of undercooling at the solid/liquid interface and decrease the extent of the undercooled liquid zone. So that, it can be qualitatively estimated that the sluggish diffusion effect of HEAs could facilitate the suppression of CET. Furthermore, higher G promotes the formation of columnar crystals. And G of the molten pool of HSLC could be estimated to be about 10^6–10^8 K/m, higher by one order of magnitude than traditional laser cladding [56], since a micron-scale molten pool could be formed in HSLC with a relatively high melting point (2196 K for $Al_{0.2}CrNbTiV$). In the research of Meng [61] and Tai [63], et al., the laser processing AlCoCrCuFeNi coating exhibited columnar crystals dominant structure [61,63] with a temperature gradient of 3×10^6 K/m. Therefore, under the combination effect of

ultra-high temperature gradient of HSLC and sluggish diffusion of HEAs, columnar dendrites dominant solidification structure could be formed in LC1.5 and LC2.0. At the same time, in the modified Hunt's model for laser processing treatment [76], the volume fraction of equiaxed crystals depends on G and V, high G and/or low R have a tendency to suppress the CET. So that, LC1.5 with lower G could have the chance to form more proportion of equiaxed grains, identical with the SEM results in Fig. 8.

3.4. EBSD analysis of $Al_{0.2}CrNbTiV$ coatings with different dilution

To further confirm the phase structure of the coatings with different dilution deposited by HSLC, the EBSD measurement is performed, with EBSD BC images (band contrast figure), IPF (inverse pole figure) maps and corresponding SEM image shown in Fig. 9, here, [0 0 1] is designated as the reference direction for the inverse pole figure to code the
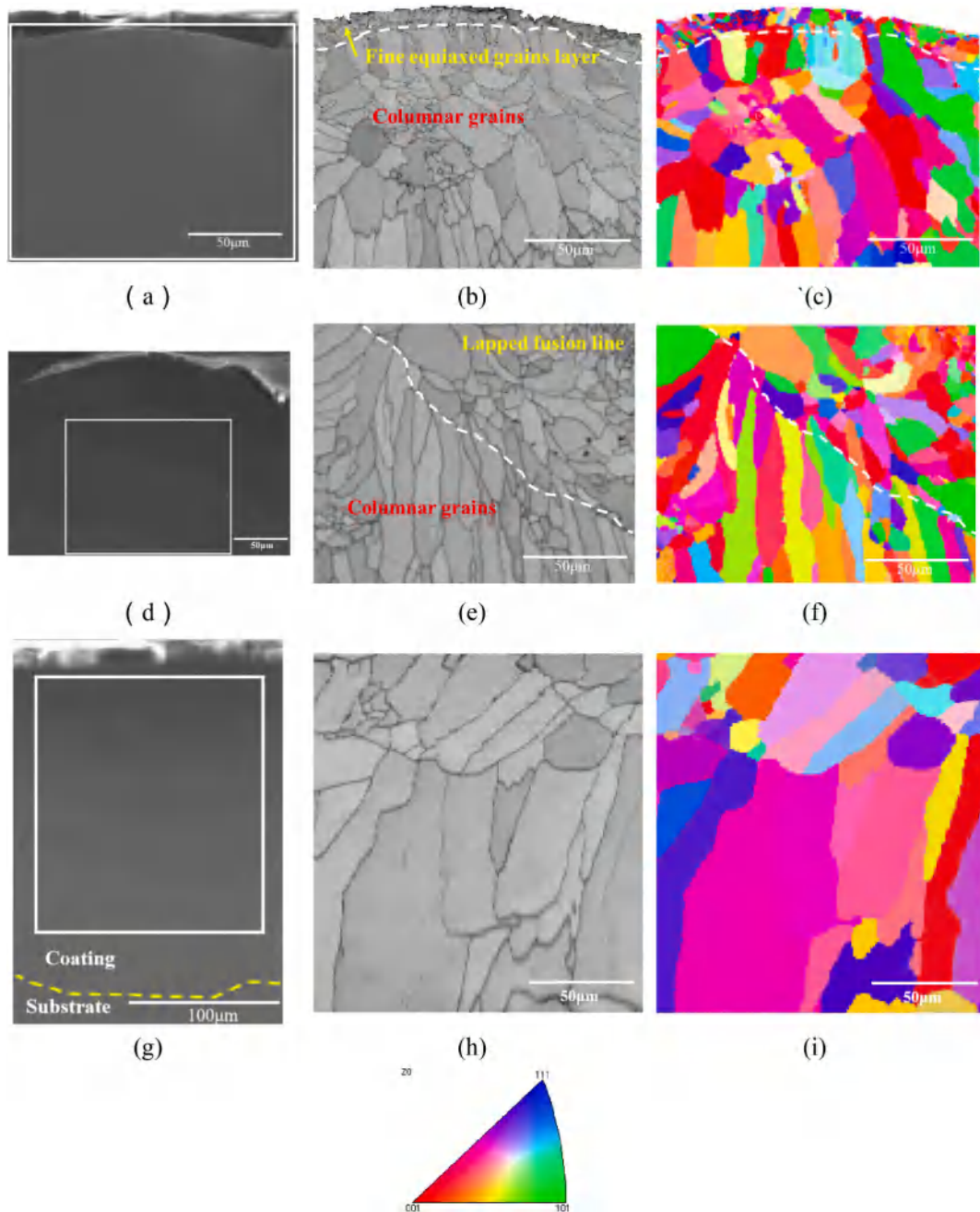
Fig. 9. EBSD image of $Al_{0.2}CrNbTiV$ coating: (a) (d) (f) SEM figure, (b) (e) (h) band contrast figure and (c) (f) (i) inverse pole figure with (a) (b) (c) represents the surface-middle part of LC1.5, (a) (b) (c) represents the middle-bottom part of LC1.5 and (g) (h) (i) LC2.0.

color pattern, as indicated by the triangle. Both the coatings possess columnar dominant grains, consistent with the SEM results. Furthermore, more unidirectional grain growth is formed in LC2.0 with higher G, and grains near the coating surface exhibits characteristics of epitaxial growth (seen in Fig. 9 g–i), whereas, fine equiaxed grains layer with the thickness of ~5.6 μm is formed near the coating surface for LC1.5 (seen in Fig. 9 a–c), confirm the analysis of solidification behavior further.

The columnar grains have an aspect ratio of ~4.88 and ~3.14, in width of ~21.5 μm, ~8.19 μm for LC2.0 and LC1.5, respectively, indicating coating with different dilution exhibits different grain growth pattern, and higher G of LC2.0 prompts the growth of columnar grains. And the smaller grain size of LC1.5 is the result of the combination effect of heat input and lattice distortion. On the one hand, the higher solidification rate of LC1.5 under lower heat input has a stronger inhibit effect on grain growth. On the other hand, the lattice distortion of the BCC solid solution in LC1.5 with lower dilution is more sever, which could enhance the solid solution strengthening effect, and prevent the grain growth, since Ti has a closely atomic radius with Al and Nb, and the lattice distortion energy caused by the difference of atomic size could get released with the dissolve of large amount of Ti elements in LC2.0. The calculated atomic differences δ with 6.14 % for LC1.5and 5.93 % for LC2.0 (seen in Table 3) also confirm more severe lattice distortion exists in LC1.5. Furthermore, the lattice distortion energy is even greater than the grain boundary energy [77], so that LC1.5 has smaller grain size under the greater resistance to grain growth. Noted that, lapped fusion "line" could also be observed in the EBSD image (seen in Fig. 9 d–f), consistent with the SEM analysis result (shown in Fig. 8 e–f), coarser equiaxed grains are formed there, and columnar grains keep growing along heat flow direction below this region.

It is interesting to find that the grain morphology in Fig. 9 is not the same as the SEM observation in Fig. 8, which transforms to coarser directional solidified grains in the EBSD images. The reason is that SEM image is formed mainly attributed to the component segregation, whereas, EBSD map more relies on the crystal structure and growth orientation [11]. Therefore, grains have similar phase structure and growth orientation cannot be distinguished with some grain boundary almost disappeared, and coarser directional solidified grains are easier to be observed in the EBSD map, which have been proved in the research of Zhang et al. [11,78].

Kernel average misorientation (KAM) diagram reflected the plastic deformation degree of grains qualitatively (seen in Fig. 10), which could be used to estimate the geometrically necessary dislocation density using the Frank's equation [36] in Eq. (9), as the local orientation difference is consistent with the geometrically necessary dislocation density [79,80].

$$\rho = \frac{2KAM_{ave}}{b \times h} \tag{9}$$

where ρ is the dislocation density, KAM_{ave} represents the KAM's weighted average for the selected region, b represents the Burgers vector and h is the step size during EBSD scanning. The mean KAM values of LC1.5 and LC2.0 are shown in Fig. 10c. The calculated geometrically necessary dislocation densities of LC1.5 and LC2.0 are 1.29×10^{13} m^{-2} and 6.61×10^{12} m^{-2} respectively. The reason is that during the solidification and crystallization process, dislocation will be consumed to form the crystalline core, and greater amount of dislocation will be left in LC1.5 since higher cooling rate could decelerate the transformation of the dislocation.

Geometrically necessary dislocation [80] is the dislocation associated with the long-range distortion gradient in the material, and the accumulation of dislocations would impede the movement of material in the slip system. Since plastic deformation is mainly accomplished through slip, the dislocation density will play an important role in the hardening process, and high resistance caused by dislocation accumulation must be overcome for plastic deformation to occur [32]. Thus, LC1.5 will show better plastic deformation resistance than LC2.0. Meanwhile, higher dislocation density would lead to higher stress concentration with increasing external force [32].

Schmid factor diagram of LC1.5 and LC2.0 is displayed in Fig. 11. It has been reported, Schmid factor for soft grains is >0.4 with grain's color near to read, while the value for hard grains is lower than 0.35 [32]. And the Schmid factor distribution in Fig. 11c reflects that LC2.0 has a higher percentage of soft grains (89.06 % for LC1.5 and 94.28 % for LC2.0), that is, Schmid factor is higher in LC2.0. Therefore, the plastic deformation is easier to occur in LC2.0.

3.5. Mechanical properties of Al$_{0.2}$CrNbTiV coatings with different dilution

Nano-indentation test is used to accurately measure the mechanical properties of coatings, and the load-displacement curves with succession loading and unloading stages are depicted in Fig. 12a, the nanohardness and modulus calculated through the Oliver& Pharr method [81] are shown in Table 6. In response to 9 mN indentation load, LC1.5 exhibits a smaller penetration depth of 192.82 nm, while LC2.0 is 203.97 nm, and the hardness at maximum load is 6.45 GPa for LC1.5 and 5.89 GPa for LC2.0, respectively. Both the Nanohardness of LC 1.5 and LC2.0 is higher than the TC4 substrate (~2.84 GPa), suggesting that the HEA coatings are more resistant to plastic deformation than the titanium

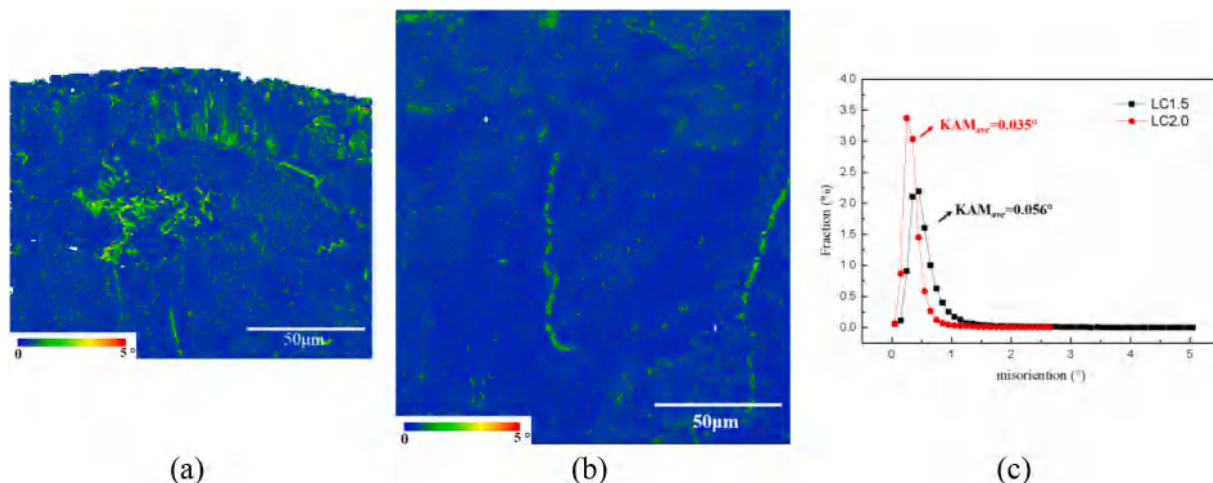**Fig. 10.** KAM map of Al$_{0.2}$CrNbTiV coating (a)LC1.5; (b) LC2.0; (c) KAM distribution.
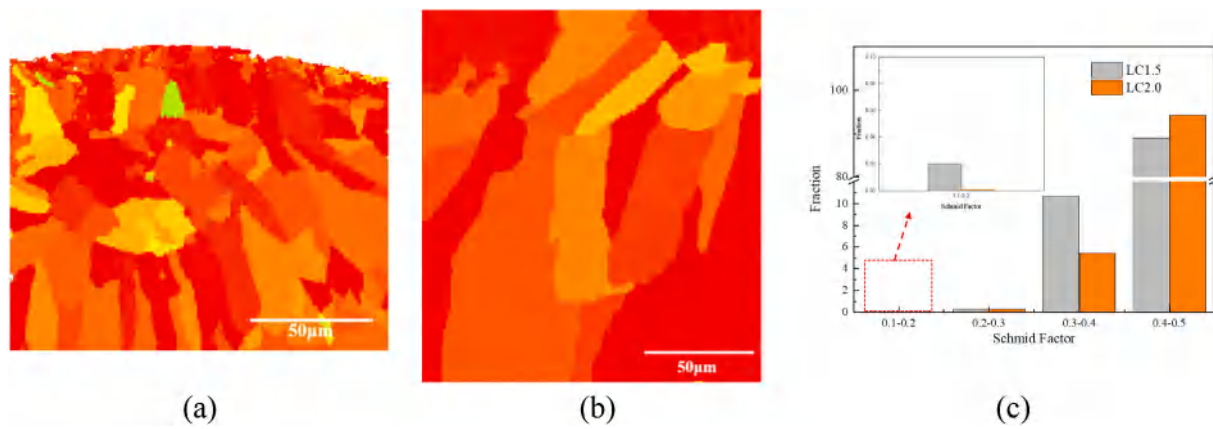
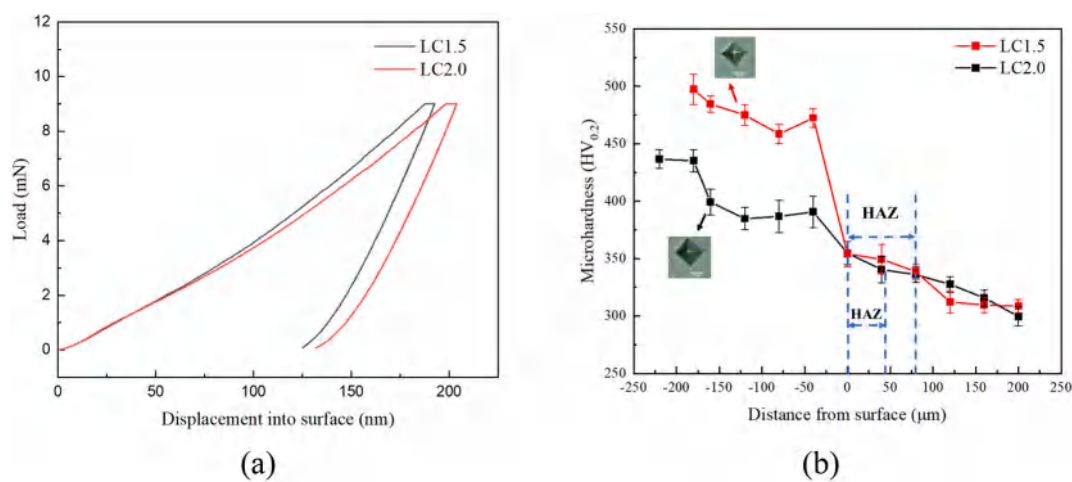**Fig. 11.** Schmid factor map of $Al_{0.2}CrNbTiV$ coating (a)LC1.5; (b) LC2.0; (c) Schmid factor distribution.

Fig. 12. Load-displacement curves (a) and the microhardness distribution (b) of $Al_{0.2}CrNbTiV$ coatings.

Table 6
Mechanical properties of $Al_{0.2}CrNbTiV$ coatings.

Coating	Max displacement (nm)	Nano-hardness at max load (H/GPa)	Modulus at max load (Er/GPa)	H/Er	H^3/Er^2 (GPa)	$1/Er^2H$ $(GPa^{-3}) \times 106$
LC1.5	192.82 ± 1.21	6.45 ± 0.1	134.57 ± 1.13	0.048	0.015	8.56
LC2.0	203.97 ± 3.14	5.89 ± 0.2	127.12 ± 1.37	0.046	0.012	10.50

substrate, attributed to the BCC strengthening phase and the lattice distortion effect of the HEA coating [82,83].

Consistent with the EBSD analysis, the plastic deformation resistances of the BCC phase in LC1.5 is higher than that of in LC2.0. That is, under the same load, greater indentation depth could be obtained for LC2.0. And both solid solution strengthening and grain-boundary hardening effect contribute to the high hardness of LC1.5 [84]. The grain boundary strengthening effect can be described using the well-known Hall-Petch relationship as: $\Delta H_G = \frac{k}{\sqrt{d}}$, where k is a material constant and d is the grain size, which indicates the hardness will get enhanced with the decreasing of the grain size. The reason is that grain boundaries could act as strong obstacles to the dislocation motion. So that plastic deformation resistance get improved more greatly in LC1.5 with smaller grain size. Furthermore, when dislocation moves along the plane with smaller crystallite size, the slip resistance and lattice distortion is greater [10,85]. Hence, the smaller grains help to enhance the hardness of LC1.5. At the same time, one of the most important intrinsic features of HEA is the great lattice distortion caused by the mixing of multicomponents with nearly equiatomic ratio [39,86]. The

heavily dilution of LC2.0 leads to large amounts of Ti dissolved in the coating, and reduce the degree of lattice distortion, instead, severe lattice distortion exists in LC1.5 with lower dilution. Therefore, under the enhancement fine grain strengthening effect and solid solution strengthening effect, LC 1.5 exhibits higher hardness. And the dissolve of large amount of "soft" Ti element also contribute to the decrease of hardness for LC2.0. In the research of Dada et al. [83], coating with decreasing laser energy also showed higher hardness.

The microhardness distribution of the coatings is plotted in Fig. 12b, and the average microhardness of LC1.5, LC2.0 is $477HV_{0.2}$ and $405HV_{0.2}$, respectively. The value of nanohardness is a little higher, that is the elasticity of materials get enhancement under weaker loads. And this phenomenon should be related with the real physical effect of superelastic behavior under mN scale forces, due to the inactivation of dislocations [88,89]. It may also be an artefact due to the piling-up of the surface during indentation [87]. Meanwhile, Fig. 12b reveals that the hardness near the coating surface is a little higher than other regions, which may be related with the fine grain strengthening mechanism. And the fluctuation of the hardness could be contributed to the exist of the lapped fusion "line" with coarser grains. The heat affected zone (HAZ) of

coating LC1.5 is ~33 μm, while LC2.0 possessed a broader HAZ of ~76 μm with greater heat input.

Elastic modulus is an important parameter for the structural performance of alloys, which reflects the strength of bonds between atoms, ions, or molecules and the ability of a material to resist elastic deformation [32,90]. The elastic modulus is 134.57 GPa for LC1.5 and 127.12 GPa for LC2.0. The higher the elastic modulus, the greater the stiffness, the more difficult for the material to deform elastically, and the brittleness will get increased as well [32,90]. Therefore, LC2.0 have lower stiffness and brittleness, that is LC2.0 will exhibit higher flexibility and elastic deformation during deformation process.

The relationship between nanohardness (H) and effective elastic modulus (Er) can be represented by wear resistance (H/Er [91]), resistance to plastic deformation (H^3/Er^2), [92], and resistance to crack damage ($1/Er^2 \cdot H$) [64,93,94]. Both the H/Er and H^3/Er^2 parameter of LC1.5 get increased compared to LC2.0, indicating the high dilution enables poor wear resistance, resistance to plastic deformation as well as the lower hardness, consistent with the EBSD analysis. It is also found that the resistance to crack damage ($1/Er^2 \cdot H$) somewhat decreased in LC1.5.

4. Conclusions

The lightweight $Al_{0.2}CrNbTiV$ RHEAs coatings were successfully produced using HSLC. The RHEA coatings in thickness of ~150–450 μm are almost free of defects and controllable in dilution (~3–35 %) with a very minimal transition zone of <10 μm. The effect of the dilution was discussed, and the microstructure and mechanical properties of the coatings with typical dilution (3.1 % of LC1.5 and 31.9 % of LC2.0) were intensively studied, and main findings were summarized as follows:

(1) The dilution of coating strongly depended on the specific energy density (K) and specific powder density (M), and coating with feasible dilution (<10 %) could be deposited through the control of K and M.

(2) HSLC facilitated the formation of disordered solid solution, and coatings in varying dilution kept simple BCC structure. S—K criterion of S < 6.5 kJ/g, $3.85 \leq K \leq 140$ J/mm^2 was proposed for HSLC to obtain simple solid solution structured coating in low dilution.

(3) The RHEA coatings produced by HSLC had fine columnar dominant structure under the combination effect of ultra-high temperature gradient and sluggish diffusion of HEAs, and coating with higher dilution showed a stronger tendency for epitaxial growth.

(4) LC1.5 in lower dilution had smaller grain size but higher dislocation density under lower heat input, and it exhibited higher hardness under the solid solution and grain-boundary hardening effect, with the resistance to plastic deformation also got improved.

CRediT authorship contribution statement

Li-Yan Lou: Data curation, Writing – review & editing, Methodology. **Kang-Cheng Liu:** Investigation. **Yun-Jie Jia:** Visualization. **Gang Ji:** Investigation. **Wei Wang:** Data curation. **Chang-Jiu Li:** Supervision. **Cheng-Xin Li:** Resources, Conceptualization.

Uncited references

[54,55,92]

Declaration of competing interest

We declare that we have no financial and personal relationships with other people or organizations that can inappropriately influence our work. There is no professional or other personal interest of any nature or kind in any product, service or company that could be construed as influencing the position presented in, or the review of, the manuscript entitled "*Microstructure and properties of lightweight Al$_{0.2}$CrNbTiV RHEA coating with different dilutions deposited by high speed laser cladding*".

Data availability

The authors do not have permission to share data.

References

[1] O.N. Senkov, G.B. Wilks, D.B. Miracle, et al., Refractory highentropy alloys, Intermetallics 18 (9) (2010) 1758–1765.

[2] S. Sheikh, L. Gan, A. Ikeda, et al., Alloying effect on the oxidation behavior of a ductile Al0.5Cr0.25Nb0.5Ta0.5Ti1.5 refractory high-entropy alloy, Mater. Today Adv. 7 (100104) (2020).

[3] O.N. Senkov, G.B. Wilks, J.M. Scott, et al., Mechanical properties of Nb25Mo25Ta25W25 and V20Nb20Mo20Ta20W20 refractory high entropy alloys, Intermetallics 19 (2011) 698–706.

[4] O.N. Senkov, J.M. Scott, S.V. Senkova, et al., Microstructure and room temperature properties of a high-entropy TaNbHfZrTi alloy, J. Alloys Compd. 509 (2011) 6043–6048.

[5] L.Y. Lou, S.N. Chen, Y. Liu, et al., Microstructure and mechanical properties of lightweight AlxCrNbTiV(x = 0.2, 0.5, 0.8) refractory high entropy alloys, International Journal of Refractory Metals and Hard Materials. 104 (2022) 105784.

[6] J. Kuainski, S. Kac, A. Kopia, et al., Laser modification of the materials surface layers review, Bull. Pol. Acad. Sci. 60 (4) (2012) 711–728.

[7] X.R. Zhang, X.F. Cui, G.J. Jin, et al., Microstructure evolution and properties of NiTiCrNbTax refractory high-entropy alloy coatings with variable ta content, J. Alloys Compd. 891 (2022), 161756.

[8] M.N. Zhang, X.L. Zhou, X.N. Yu, et al., Synthesis and characterization of refractory TiZrNbWMo high-entropy alloy coating by laser cladding, Surf. Coat. Technol. 311 (2017) 321–329.

[9] Shihua Kuang, ShisongZheng FangZhou, et al., Annealing-induced microstructure and properties evolution of refractory MoFeCrTiWAlNb3 eutectic high-entropy alloy coating by laser cladding, Intermetallics 129 (2021), 107039.

[10] L. Chen, Y.Y. Wang, X.H. Hao, et al., Lightweight refractory high entropy alloy coating by laser cladding on Ti–6Al–4V surface, Vacuum 183 (2021), 109823.

[11] Q. Chao, T.T. Guo, T. Jarvis, et al., Direct laser deposition cladding of AlxCoCrFeNi high entropy alloys on a high-temperature stainless steel, Surf. Coat. Technol. 332 (2017) 440–451.

[12] I. Hemmati, V. Ocelík, J.T.M. De Hosson, Dilution effects in laser cladding of ni-cr-B-si-C hardfacing alloys, Mater. Lett. 84 (2012) 69–72.

[13] X. Li, Y. Feng, B. Liu, et al., Influence of NbC particles on microstructure and mechanical properties of AlCoCrFeNi high-entropy alloy coatings prepared by laser cladding, J. Alloys Compd. 788 (2019) 485–494.

[14] J. Liu, H. Liu, P. Chen, J. Hao, Microstructural characterization and corrosion behaviour of AlCoCrFeNiTix high-entropy alloy coatings fabricated by laser cladding, Surf. Coat. Technol. 361 (2019) 63–74.

[15] Y.Q. Jiang, J. Li, Y.F. Juan, et al., Evolution in microstructure and corrosion behavior of AlCoCrxFeNi high-entropy alloy coatings fabricated by laser cladding, J. Alloys Compd. 775 (2019) 1–14.

[16] T. Schopphoven, A. Gasser, K. Wissenbach, Investigation on ultrahigh-speed laser material deposition as alternative for hard chrome plating and thermal spraying, J. Laser Appl. 28 (2) (2016), 002501-1–002501-9.

[17] T. Schopphoven, A. Gasser, G. Backes, EHLA: extreme high-speed laser material deposition-economical and effective protection against corrosion and wear, Laser Technik J. 4 (2017) 26–29.

[18] Q.L. Xu, Y. Zhang, S.H. Liu, et al., High-temperature oxidation behavior of CuAlNiCrFe highentropy alloy bond coats deposited using high-speed laser cladding process, Surf. Coat. Technol. 398 (2020), 126093.

[19] C. Lampa, I. Smirnov, High speed laser cladding of an iron based alloy developed for hard chrome replacement, J. Laser Appl. 31 (2019), 022511.

[20] L.Q. Li, F.M. Shen, Y.D. Zhou, et al., Microstructure and corrosion resistance analysis of 431 stainless steel coating prepared by extreme high speed laser cladding and conventional laser cladding, Chin. J. Lasers 46 (10) (2019) 174–183.

[21] O. Asghar, L.Y. Lou, M. Yasir, et al., Enhanced tribological properties of LA43M magnesium alloy by Ni60 coating via ultra-high-speed laser cladding, Coatings 10 (638) (2020) 1–14.

[22] L.Y. Lou, Y. Zhang, Y.J. Jia, et al., High speed laser cladded Ti-Cu-NiCoCrAlTaY burn resistant coating and its oxidation behavior, Surf. Coat. Technol. 392 (2020), 125697.

[23] C.C. Du, L. Hu, X.D. Ren, et al., Cracking mechanism of brittle FeCoNiCrAl HEA coating using extreme high-speed laser cladding, Surf. Coat. Technol. 424 (2021), 127617.

[24] S. Zhang, C.L. Wu, C.H. Zhang, et al., Laser surface alloying of FeCoCrAlNi high-entropy alloy on 304 stainless steel to enhance corrosion and cavitation erosion resistance, Opt. Laser Technol. 84 (2016) 23–31.

[25] T. Schopphoven, A. Gasser, K. Wissenbach, Investigations on ultra-high-speed laser material deposition as alternative for hard chrome plating and thermal spraying, J. Laser Appl. 28 (2) (2016), 022501-1–022501–9.

[26] X. Wu, B. Zhu, X. Zeng, et al., Critical state of laser cladding with powder auto-feeding, Surf. Coat. Technol. 79 (1996), 200204.

[27] B. Song, T. Hussain, K.T. Voisey, Laser cladding of Ni50Cr: a parameter and dilution study, Phys. Procedia 83 (2016) 706–715.

[28] G.J. Bruck, Fundamentals and industrial application of high power laser beam cladding, in: Laser Beam Surface Treating and Coating 957, 1988, pp. 14–28.

[29] Ehsan Toyserkani, Amir Khajepour, Stephen Corbi, Laser Cladding, CRC Press, 2005.

[30] U. De Oliveira, V. Ocelík, J.T.M. De Hosson, Analysis of coaxial laser cladding processing conditions, Surf. Coat. Technol. 197 (2005) 127–136.

[31] M.K. Alam, A. Edrisy, J. Urbanic, Microstructural analysis of the laser-cladded AISI 420 martensitic stainless steel, Metall. Mater. Trans. A 20 (2019) 2495–2506.

[32] Y. Cui, J.Q. Shen, S. Marwan, et al., Strengthening mechanism in two-phase FeCoCrNiMnAl high entropy alloy coating, Appl. Surf. Sci. 530 (2020), 147205.

[33] R.D. Li, P.D. Niu, T.C. Yuan, et al., Selective laser melting of an equiatomic CoCrFeMnNi high-entropy alloy: processability, non-equilibrium microstructure and mechanical property, J. Alloys Compd. 746 (2018) 125–134.

[34] Y.F. Juan, J. Li, Y.Q. Jiang, et al., Modified criterions for phase prediction in the multi-component laser-clad coatings and investigations into microstructural evolution/wear resistance of FeCrCoNiAlMox laser-clad coatings, Appl. Surf. Sci. 465 (2019) 700–714.

[35] U. Mizutani, Hume-rothery rules for structurally complex alloy phases, MRS Bull. 37 (02) (2012) 169.

[36] M. Calvo-Dahlborg, S.G.R. Brown, Hume-rothery for HEA classification and selforganizing map for phases and properties prediction, J. Alloys Compd. 724 (2017) 353–364.

[37] S. Guo, C. Ng, J. Lu, et al., Effect of valence electron concentration on stability of fcc or bcc phase in high entropy alloys, J. Appl. Phys. 109 (2011), 103505.

[38] H. Zhang, Y. Pan, Y.Z. He, et al., Microstructure and properties of 6FeNiCoSiCrAlTi high-entropy alloy coating prepared by laser cladding, Appl. Surf. Sci. 257 (2011) 2259–2263.

[39] Y. Zhang, Y.J. Zhou, J.P. Lin, et al., Solid solution phase formation rules for multi-component alloys, Adv. Eng. Mater. 10 (2008) 534–538.

[40] X. Yang, Y. Zhang, Prediction of high-entropy stabilized solid-solution in multi-component alloys, Mater. Chem. Phys. 132 (2012) 233–238.

[41] S. Guo, C.T. Liu, Phase stability in high entropy alloys: formation of solid-solution phase or amorphous phase, Prog. Nat. Sci. Mater. Int. 21 (2011) 433–446.

[42] Q.F. Ye, K. Feng, Z.G. Li, et al., Microstructure and corrosion properties of CrMnFeCoNi high entropy alloy coating, Appl. Surf. Sci. 396 (2017) 1420–1426.

[43] S. Zhang, C.L. Wu, C.H. Zhang, Phase evolution characteristics of FeCoCrAlCuVxNi high entropy alloy coatings by laser high-entropy alloying, Mater. Lett. 141 (2015) 7–9.

[44] H. Zhang, W.F. Wu, Y.Z. He, et al., Formation of core-shell structure in high entropy alloy coating by laser cladding, Appl. Surf. Sci. 363 (2016) 543–547.

[45] M.H. Sha, L. Zhang, J.W. Zhang, et al., Effects of annealing on the microstructure and wear resistance of AlCoCrFeNiTi0.5 high-entropy alloy coating prepared by laser cladding, Rare Metal Mater. Eng. 46 (2017) 1237–1240.

[46] Y.X. Guo, X.J. Shang, Q.B. Liu, Microstructure and properties of in-situ TiN reinforced laser cladding CoCr2FeNiTix high-entropy alloy composite coatings, Surf. Coat. Technol. 344 (2018) 353–358.

[47] F.Y. Shu, L. Wu, H.Y. Zhao, et al., Microstructure and high-temperature wear mechanism of laser cladded CoCrBFeNiSi high-entropy alloy amorphous coating, Mater. Lett. 211 (2018) 235–238.

[48] G. Jin, Z.B. Cai, Y.J. Guan, et al., High temperature wear performance of laser-cladded FeNiCoAlCu high-entropy alloy coating, Appl. Surf. Sci. 445 (2018) 113–122.

[49] H.W. Chang, P.K. Huang, J.W. Yeh, et al., Influence of substrate bias, deposition temperature and post-deposition annealing on the structure and properties of multi-principal-component (AlCrMoSiTi)N coatings, Surf. Coat. Technol. 202 (14) (2008) 3360–3366.

[50] L.H. Wen, H.C. Kou, J.S. Li, et al., Effect of aging temperature on microstructure and properties of AlCoCrCuFeNi high-entropy alloy, Intermetallics 17 (4) (2009) 266–269.

[51] W.J. Boettinger, M.J. Aziz, Theory for the trapping of disorder and solute in intermetallic phases by rapid solidification, Acta Metall. 37 (1989) 3379–3391.

[52] Q. Zhang, M.Y. Li, B. Han, Investigation on microstructures and properties of Al1.5CoCrFeMnNi high entropy alloy coating before and after ultrasonic impact treatment, J. Alloys Compd. 884 (2021), 160989.

[53] Q.L. Xu, K.C. Liu, K.Y. Wang, et al., TGO and Al diffusion behavior of CuAlxNiCrFe high-entropy alloys fabricated by high-speed laser cladding for TBC bond coats, Corros. Sci. 192 (2021), 109781.

[54] Z.Q. Cui, Z. Qin, P. Dong, et al., Microstructure and corrosion properties of FeCoNiCrMn high entropy alloy coatings prepared by high speed laser cladding

[55] and ultrasonic surface mechanical rolling treatment, Mater. Lett. 259 (2020), 126769.

[55] H.J. Wang, W. Zhang, Y. Peng, et al., Microstructures and wear resistance of FeCoCrNi-Mo high entropy alloy/diamond composite coatings by high speed laser cladding, Coatings 10 (2020) 300.

[56] M. Gaumann, C. Bezencon, P. Canalis, et al., Singal-crystal laser deposition of superalloys: processing- microstructure maps, Acta Mater. 49 (2001) 1051–1062.

[57] W. Kurz, B. Giovanola, R. Trivedi, Theory of microstructure development during rapid solidification, Acta Mater. 34 (5) (1986) 823–830.

[58] Yinuo Guo, Haijun Sua, Haotian Zhou, et al., Unique strength-ductility balance of AlCoCrFeNi2.1 eutectic high entropy alloy with ultra-fine duplex microstructure prepared by selective laser melting, J. Mater. Sci. Technol. 111 (2022) 298–306.

[59] Y. Liu, C.X. Li, X.F. Huang, et al., Investigation on solidification structure and temperature field with novel processing of synchronous powder-feeding underwater laser cladding, J. Mater. Process. Technol. 296 (2021), 117166.

[60] L.Y. Lou, Y. Zhang, Q.L. Xu, et al., Microstructure and properties of metallic coatings with low dilution ratio by high speed laser cladding, China Surf. Eng. 33 (2) (2020) 149–159.

[61] G.H. Meng, N.A. Protasova, E.P. Kruglov, et al., Solidification behavior and morphological evolution in laser surface forming of AlCoCrCuFeNi multi-layer high-entropy alloy coatings on AZ91D, J. Alloys Compd. 772 (2019) 994–1002.

[62] T.M. Yue, H. Xie, X. Lin, et al., Solidification behaviour in laser cladding of AlCoCrCuFeNi high-entropy alloy on magnesium substrates, J. Alloys Compd. 587 (2014) 588–593.

[63] Y. Tai, H. Xie, X. Lin, et al., Microstructure of laser remelted AlCoCrCuFeNi high entropy alloy coatings produced by plasma spraying, Entropy 15 (2013) 2833–2845.

[64] C.H. Sha, Z.F. Zhou, Z.H. Xie, et al., High entropy alloy FeMnNiCoCr coatings: enhanced hardness and damagetolerance through a dual-phase structure and nanotwins, Surf. Coat. Technol. 385 (2020), 125435.

[65] Y. Jiang, Y. Cheng, X. Zhang, et al., Simulation and experimental investigations on the effect of Marangoni convection on thermal field during laser cladding process, Optik 203 (2020), 164044.

[66] N.D. Stepanov, N.Yu Yurchenko, D.V. Skibin, et al., Structure and mechanical properties of the AlCrxNbTiV (x 1/4 0, 0.5, 1,1.5) high entropy alloys, J. Alloys Compd. 652 (2015) 266–280.

[67] N.Yu. Yurchenko, N.D. Stepanov, A.O. Gridneva, et al., Effect of Cr and Zr on phase stability of refractory Al-Cr-Nb-Ti-V-Zr high-entropy alloys, J. Alloys Compd. 757 (2018) 403–414.

[68] N.D. Stepanov, D.G. Shaysultanov, , et al.N.Yu. Yurchenko, Effect of Al content on structure and mechanical properties of the AlxCrNbTiVZr (x = 0; 0.25; 0.5; 1) high-entropy alloy, Materials Characterization. 121 (2016) 125–134.

[69] B.B. Straumal, A. Korneva, A. Kuzmin, et al., The grain boundary wetting phenomena in the Ti-containing high-entropy alloys: a review, Metals 2021 (1881) 11.

[70] B.B. Straumal, P. Zie, W. Gust, Grain boundary phase transitions and phase diagrams, Int. J. Inorg. Mater. 3 (2001) 1113–1115.

[71] Z. Gu, P. Mao, Y. Gou, et al., Microstructure and properties of MgMoNbFeTi2Yx high entropy alloy coatings by laser cladding, Surf. Coat. Technol. 402 (2020), 126303.

[72] Z. Cu, S. Xi, P. Mao, et al., Microstructure and wear behavior of mechanically alloyed powder AlxMo0.5NbFeTiMn2 high entropy alloy coating formed by laser cladding, Surf. Coat. Technol. 401 (2020), 126244.

[73] A.S. Gornakova, A.B. Straumal, I.I. Khodos, et al., Effect of composition, annealing temperature, and high pressure torsion on structure and hardness of Ti-V and Ti-V-Al alloys, J. Appl. Phys. 125 (2019), 082522.

[74] M. Mukarram, M. Mujahid, K. Yaqoob, Design and development of CoCrFeNiTa eutectic high entropy alloys, J. Mater. Res. Technol. 10 (2021) 1243–1249.

[75] J.D. Hunt, Steady state columnar and equiaxed growth of dendrites and eutectic, Mater. Sci. Eng. 65 (1984) 75–83.

[76] M. Gaumann, R. Trivedi, W. Kurz, Nucleation ahead of the advancing interface ∈ in directional solidification, Mater. Sci. Eng. A 226–228 (1997) 763–769.

[77] R.Z. Tang, Physical Metallurgical Foundation, Metallurgical Industry Press, Beijing, 1997.

[78] J. Joseph, T. Jarvis, X. Wu, et al., Comparative study of the microstructures and mechanical properties of direct laser fabricated and arc-melted AlxCoCrFeNi high entropy alloys, Mater. Sci. Eng. A 633 (2015) 184–193.

[79] A.P. Zhilyaev, I. Shakhova, A. Morozova, et al., Grain refinement kinetics and strengthening mechanisms in Cu–0.3Cr–0.5Zr alloy subjected to intense plastic deformation, Mater. Sci. Eng. A 654 (2016) 131–142.

[80] Z.F. Yan, D.H. Wang, X.L. He, et al., Deformation behaviors and cyclic strength assessment of AZ31B magnesium alloy based on steady ratcheting effect, Mater. Sci. Eng. A 723 (2018) 212–220.

[81] W.C. Oliver, G.M. Pharr, Measurement of hardness and elastic modulus by instrumented indentation: advances in understanding and refinements to methodology, Journal of Materials Research. 19 (2004) 2–3.

[82] C.C. Tung, J.W. Yeh, T.T. Shun, On the elemental effect of AlCoCrCuFeNi high-entropy alloy system, Mater. Lett. 61 (1) (2007) 1–5.

[83] M. Dada, P. Popoola, N. Mathe, et al., Investigating the elastic modulus and hardness properties of a high entropy alloy coating using nanoindentation, Int. J. Lightweight Mater. Manuf. 4 (2021) 339–345.

[84] C.A. Schuh, T.G. Nieh, H. Iwasaki, The effect of solid solution W additions on the mechanical properties of nanocrystalline ni, Acta Mater. 51 (2003) 431–443.

[85] S.Y. Chen, X. Yang, K. Dahmen, et al., Microstructures and crackling noise of AlxNbTiMoV high entropy alloys, Entropy 16 (2) (2014) 870–884.

[86] Y.N. Sun, P. Chen, L.H. Liu, et al., Local mechanical properties of AlxCoCrCuFeNi high entropy alloy characterized using nanoindentation, Intermetallics 93 (2018) 85–88.

[87] C.A. Charitidis, D.A. Dragatogiannis, E.P. Koumoulos, et al., Residual stress and deformation mechanism of friction stir welded aluminum alloys by nanoindentation, Mater. Sci. Eng. A 540 (2012) 226–234.

[88] G. Cross, A. Schirmeisen, A. Stalder, et al., Adhesion interaction between atomically defined tip and sample, Phys. Rev. Lett. 80 (1998) 4685–4688.

[89] M.P. George, G.H. Erik, G. Yanfei, The indentation size effect: a critical examination of experimental observations and mechanistic interpretations, Annu. Rev. Mater. Res. 40 (2010) 271–292.

[90] S.R. Qiao, C.Y. Zhang, H. Wang, Mechanical Properties of Materials, Northwestern Polytechnical University Press, Xi'an, 2015.

[91] A. Leyland, A. Matthews, On the significance of the H/E ratio in wear control: a nanocomposite coating approach to optimised tribological behaviour, Wear 246 (2000) 1–11.

[92] M. Roy, L. Whiteside, J. Xu, et al., Diamond-like carbon coatings enhance the hardness and resilience of bearing surfaces for use in joint arthroplasty, Acta Biomater. 6 (2010) 1619–1624.

[93] A. Miserez, J.C. Weaver, P.J. Thurner, et al., Effects of laminate architecture on fracture resistance of sponge biosilica: lessons from nature, Adv. Funct. Mater. 18 (2008) 1241–1248.

[94] Y.K. Kim, J.E. Ahn, Y. Song, et al., Selective laser melted CrMnFeCoNi + 3 wt% Y2O3 high-entropy alloy matrix nanocomposite: fabrication, microstructure and nanoindentation properties, Intermetallics 138 (2021), 107319.